Structural, Morphological and Textural Properties of Iron Manganite ($FeMnO_3$) Thick Films Applied for Humidity Sensing

Maria Vesna Nikolic[1*], Jugoslav. B. Krstic[2], Nebojsa J. Labus[3], Miloljub D. Lukovic[1], Milena P. Dojcinovic[1], Milan Radovanovic[4], Nenad B. Tadic[5]

[1]Institute for Multidisciplinary Research, University of Belgrade, Kneza Viseslava 1, 11030 Belgrade, Serbia

[2]Institute of Chemistry, Technology and Metallurgy, Department of Catalysis and Chemical Engineering, University of Belgrade, Serbia

[3]Institute of Technical Sciences of SASA, Belgrade, Serbia

[4]University of Novi Sad, Faculty of Technical Sciences, Novi Sad, Serbia

[5]University of Belgrade, Faculty of Physics, Belgrade, Serbia

*corresponding author: mariav@rcub.bg.ac.rs

Abstract

Iron manganite ($FeMnO_3$) powder with a cubic (bixbyite, $\boldsymbol{Ia\bar{3}}$) crystal structure was obtained by a solid state reaction. Thick film paste (powder + organic vehicles) was screen printed on alumina substrate with test interdigitated PdAg electrodes. Significant porosity (60.6%) composed of macropores (larger than 100 nm) was determined by Hg porosimetry, changing only slightly from the first extrusion run indicating a stable pore system. Hg porosimetry evaluation of thick film samples enabled estimation of true textural parameters of

the thick film compared to powder. Impedance response of the thick film sensor was monitored in a humidity chamber in the relative humidity range 30-90%, at room temperature (25^{o}C) and frequency range from 42 Hz to 1 MHz. At 100 Hz the impedance reduced from 10.41 MΩ to 0.68 MΩ for relative humidity of 30 and 90%, respectively. Analysis of complex impedance using an equivalent circuit showed the dominant influence of grain boundaries. The sensor response and recovery was fast (several seconds) and a relatively low hysteresis value of 2.8% was obtained.

Keywords: Iron manganite**;** humidity sensing,**;** mercury porosimetry; thick films; complex impedance.

1. Introduction

The Internet of Things (IoT) will soon have billions of things (sensor-enabled devices) connected to it ranging for small static devices to large and mobile devices [1, 2]. IoT devices distributed worldwide open the door to the development of Smart Cities with wireless sensor networks (WSN). Sensing platforms are one of the basic components of IoT [3]. Sensors measuring the content of different gases and humidity are essential in monitoring and detecting changes in the environment in future Smart Cities. Development of reliable, low-cost and fast sensors continues to be the subject of much research.

Metal oxide semiconductor gas sensors have been widely applied in measuring and monitoring humidity and trace amounts of environmentally important gases such as carbon monoxide and nitrogen dioxide, flammable, toxic and exhaust gases [4,5]. The advantages of these sensing materials is low cost, material abundance and ease of fabrication, though there are

some issues related to the need for periodic regeneration [6] or poor selectivity to different gases, poisoning interactions and baseline resistance drift [7]. Research continues in several directions that include investigating other oxides such as perovskites or ferrites, doping or combining different metal oxides materials forming heterostructures, heterojunctions or core-shell structures [7].

Monitoring air humidity is essential from the viewpoint of detection and control of the ambient humidity [8], while monitoring soil moisture content is very significant during irrigation [9,10]. Many different oxide systems have been investigated and applied in humidity sensing as resistive or capacitive ceramic humidity sensors. Perovskite oxides are a fascinating group of materials showing great potential in a wide range of applications, including gas and humidity sensing [11, 12]. The crystalline representations of perovskites range from cubic (high) to triclinic (low) symmetries. Some cubic perovskites, such as $SrSnO_3$, $BaSnO_3$ or $BaTiO_3$ are sensitive to humidity [13-16].

Bixbyite in the form of isometric crystals (highly modified cubes) is a mineral rarely found in nature but used as a gem. Iron manganite with a bixbyite cubic structure has been obtained by mechano-synthesis in a high energy planetary ball mill [17]. In $FeMnO_3$, Fe and Mn in the 50:50 ratio are randomly distributed over 8*a* and 24*d* sites in the $Ia\bar{3}$ cubic crystal lattice [18]. According to Kolk et al. [19] even though the unit cell is body centered cubic, the local symmetry of metal ions is non-cubic, as two sites are vacant in the cube of oxygen with metal atoms at the center. Initial investigation of iron manganite ($FeMnO_3$) in bulk form as a capacitive sensor showed that it held promise for application in humidity monitoring [20]. Analysis of the influence of humidity on complex impedance and dielectric properties of iron manganite on bulk samples showed that this material has potential for application in humidity sensing [21].

The principle of operation of ceramic oxide gas sensors is change of properties due to interaction of the surface with the surrounding atmosphere [7]. The microstructure of ceramic oxides comprises grains, grain boundaries and pores and it is closely linked to the gas sensing mechanism of these materials [4, 8]. The electrical resistance, impedance or capacitance of the material is influenced by phenomena occurring at the surface between the material (grains, grain boundaries and pores) the adsorbed oxygen ions and the target gaseous compound (water in the case of humidity) [7]. The working principle of most currently available ceramic humidity sensors is ionic conduction, where increase in relative humidity leads to increase in conductivity and the dielectric constant. Other conduction mechanisms include electronic conduction, solid electrolites and heterocontacts [14]. Regardless of the origin of impedance variation water vapor adsorption in metal oxides is based on chemisorption, physisorption and capillary condensation processes, depending on the relative humidity level [8, 14].

Screen printing is a technique used for producing commercial metal oxide gas sensors [4]. It involves printing a paste (ink) through a mesh. The paste is a mixture of the ceramic oxide powder and an organic vehicle. It is screen-printed usually on a sensor substrate most often alumina with interdigitated PdAg or gold sensing electrodes [4]. This technique is low cost and reliable. Initial investigation of the possible application of iron manganite thick films in dependence of the operating temperature (25, 50 and 75^{o}C) has shown that the highest sensitivity is observed at room temperature [22].

In this work we have analyzed the structural, morphological and textural properties of iron manganite thick films obtained by screen-printing on alumina substrate with test interdigitated electrodes and the influence of change in relative humidity (30-90%) by monitoring the change in complex impedance at room temperature (25^{o}C) in the frequency range

42 Hz – 1 MHz. The aim was to analyze potential application of $FeMnO_3$ thick films as a humidity sensor material.

2. Experimental

2.1 Materials

Hematite (α-Fe_2O_3, Sigma Aldrich) and manganese carbonate ($MnCO_3$, Sigma Aldrich) powders were mixed in the appropriate ratio. Solid state synthesis was performed and consisted of a combination of milling and calcination described in detail in [21]. Thick film paste was obtained by adding organic vehicles (ethyl cellulose as binder, α-terpineol as dispersant and ethanol) to the obtained iron manganite powder using the procedure described in detail in [23, 24]. Four layers were screen printed on test interdigitated PdAg electrodes (width 8 mm, length 10 mm and electrode spacing 0.3 mm) on an alumina substrate. Each layer was dried at 100^{o}C for 45 minutes before the next layer was printed. The iron manganite thick film sensor samples were further heat-treated at 900^{o}C for 6 h in order to burn-out organics in the thick film paste and to obtain a pure iron manganite phase on the alumina substrate. This is in accordance with literature data that a longer residence time enables the formation of a cubic $FeMnO_3$ structure with no secondary phases [20, 25]. Samples for Hall and UV-vis DRS measurements and mercury porosimetry were prepared in the same way but on plain alumina substrates (with no electrodes).

2.2 Characterization

X-ray diffraction (XRD) analyses of powder and thick film samples were performed on Philips PW 1050 and Rigaku Ultima IV diffractometers, respectively. The GSAS II package [26]

was used for structural refinement using the Rietveld method. The cubic space group $Ia\bar{3}$ was assumed with starting parameters defined in [21].

The average film thickness (of the four screen printed thick film layers) was measured on an Optical Profilometer (HRM-300 Huvitz Upright Microscope with Panasis software).

Hall measurements of thick film samples screen printed on alumina substrate were conducted at room temperature on an Ecopia HMS-Hall effect measurement system with applied field of 0.37 T and current of 1 nA.

UV-vis diffuse reflectance spectra (DRS) of powder and thick film samples were measured on a Shimadzu UV-2600 device with an ISR2600 Plus Integrating sphere attachment in the measuring range 200-1400 nm.

Scanning electron micrographs of the iron manganite powder and thick film samples were recorded on a TESCAN electron microscope VEGA TS 5130MM. The Semaphore software was used to determine the average particle size, taking into account over 300 particles.

Nitrogen adsorption-desorption isotherms of the iron manganite powder were collected on a Sorptomatic 1990 Thermo Finningen device at 77 K. Before measuring the powder samples were degassed for 36 h at 110^{o}C in vacuum.

2.3 Mercury porosimetry of powder and thick film samples

In order to investigate the porosity of the thick film layer and the influence of additional heat treatment of screen-printed thick films, we performed mercury porosimetry measurements of thick films on the alumina substrate prepared in the same way as the screen printed sensor. Typically, literature reports the results of Hg porosimetry measurements of materials used to make air humidity sensors [27-29] , in the form of powders or sintered compacts, even for

sensors made using the thick film paste screen printed technique [30]. Unfortunately, with this approach, the contribution of the thick film paste preparation process and additional heating treatment to porosity of the sensory material remains unclear, although two consecutive measurements of the peeled material (powder) from the sensor substrate (after thick film paste preparation procedure and calcinations) can be of great help [31].

The best way to determine the actual porous characteristics of the final sensor thick film using Hg porosimetry involves measuring the sensor material deposited on a support of known porous characteristics. The porous characteristics of the support may be determined either by separate measurement of the support, or by blank measurement of the sample holder (dilatometer) itself normally conducted before actual measurement of any sample to determine the compressibility of mercury and the compressibility of all elements of the sample holder. In our case, the second approach was applied because a non-porous alumina plate with a total pore volume below 0.4 mm^3/g (porosity less than 0.2%) was selected as the support.

Mercury porosimetry measurements of $FeMnO_3$ powders (synthesized powder and powder additionally calcined at 900 ^oC for 6 h) and thick film samples (thick film paste screen printed on an alumina substrate thermally treated at 900 ^oC for 6 h), were performed with a high-pressure units PASCAL (Thermo) in a pressure range of 0.1-200 MPa. Four thick film samples were prepared by screen printing 4 layers of thick film (as described above) on plain alumina substrate. They were broken into pieces 3 mm x 14 mm to be able to be put into the CD3-P type dilatometer. The SOLID Software System PC interface was used for automatic data acquisition and textural parameters calculation.

Before individual analysis the samples (powder or thick film on alumina support) were dried at 110 ºC 4h in an oven and additionally evacuated for 2 h inside the sample holder at the

analytical position of a Macropore Unit 120 (Carlo Erba), which was used for mercury filing of the dilatometer and bulk density determination.

2.4 Humidity sensing

The influence of change in the relative humidity (RH) in the range 30-90% at room temperature on sensor complex impedance ($Z = R + jX$) was monitored in a JEIO TECH TH-KE 025 temperature and humidity climatic chamber in the frequency range from 42 Hz to 1 MHz on a HIOKI 3532-50 LCR HiTESTER device at room temperature (25 ^{o}C). Absorption (relative humidity increasing from 30 to 90%) and desorption (relative humidity decreasing from 90 to 30%) were measured in order to determine hysteresis curves that define the time delay between absorption and desorption processes.

3. Results and Discussion

3.1 Thick film structure, carrier mobility and optical properties

An example of an iron manganite thick film sample and alumina substrate with test electrodes is shown in Fig. 1.

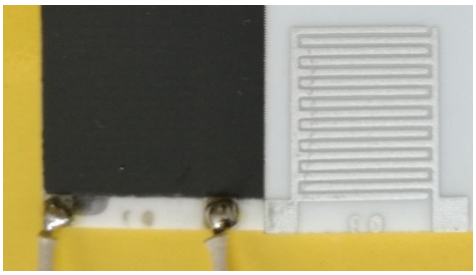

Fig. 1 Iron manganite thick film sample (left) and alumina substrate with test PdAg electrodes (right)

The screen printed film thickness was determined to be about 55 µm as shown in Fig. 2. This is in accordance with previous estimations of screen printed film thickness of 12-15 µm from FESEM images of the thick film cross section [24], where the thickness of four layers would be between 48 and 60 µm.

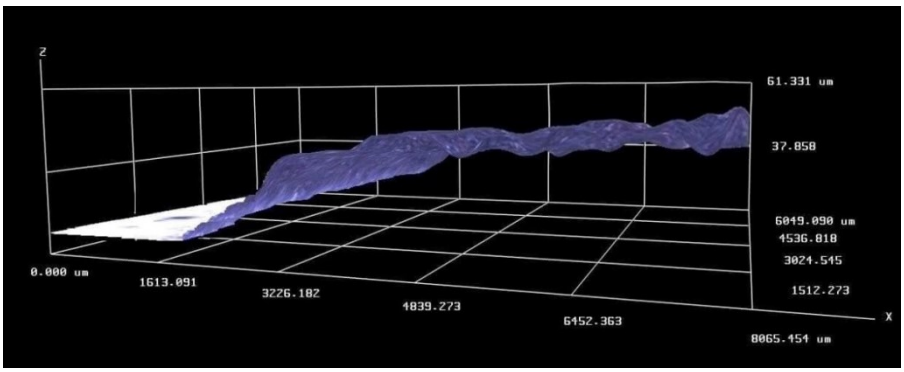

Fig. 2 Optical profilometer image of thick film sample, film thickness estimated 55 µm

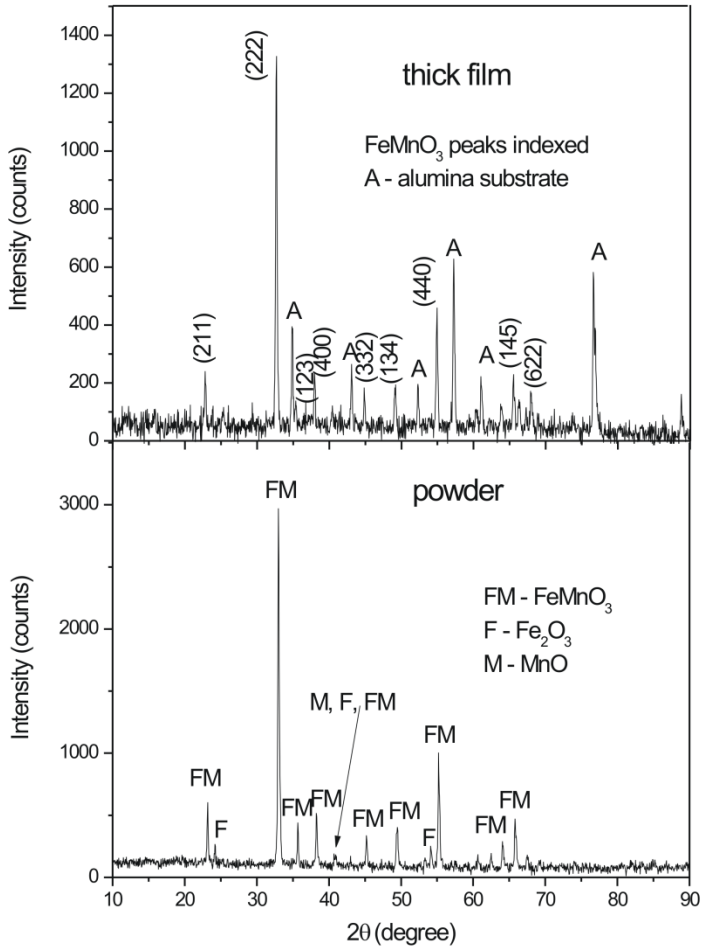

Fig. 3 X-ray diffraction pattern of iron manganite powder and thick film sample

X -ray diffraction patterns of the obtained powder (Fig. 3) showed that it consisted of $FeMnO_3$ with a cubic $Ia\bar{3}$ structure (a = 9.4028(5) Å, crystallite size: 316 nm, microstrain: $4.9(3)\cdot10^{3}$) and a small amount of unreacted hematite (α-Fe_2O_3) and possible traces of manganese oxide. Peaks of unreacted hematite have been noted before in iron manganite produced by mechanical alloying [32], ball milling [33] or co-precipitation [34]. XRD analysis of $FeMnO_3$ thick film samples showed that after sintering at 900^{o}C for 6 hours only iron

manganite ($FeMnO_3$) with a cubic $Ia\bar{3}$ structure (a = 9.389(4) Å) remained, as shown in Fig. 3. Peaks belonging to the alumina substrate were also noted and marked.

Hall effect measurements with an input current of 1 nA and applied field of 0.37 T at room temperature enabled determination of carrier mobility $\mu = 55.18$ $cm^2/V{\cdot}s$, bulk concentration $N_b = 2.556{\cdot}10^{10}$ cm^{-3}, resistivity $4.426{\cdot}10^6$ Ω·cm and average Hall coefficient $2.422{\cdot}10^8$ cm^3/C.

The optical band gap of the obtained iron manganite powder and thick film sample was estimated from the Kubelka-Munk transformation of the measured DRS spectra (Fig. 4). It was 1.63 eV for the powder and 1.41 eV for the thick film sample. These values are lower than the value of 1.901 eV determined by Habibi and Mosavi for iron manganite nanopowder obtained using the coprecipitation method [35]. These variations can be due to differences in powder morphology and particle size. In our case the iron manganite powder contained small amounts of unreacted hematite and manganese oxide that possibly accounted for the difference in optical band gap values between the powder and thick film sample.

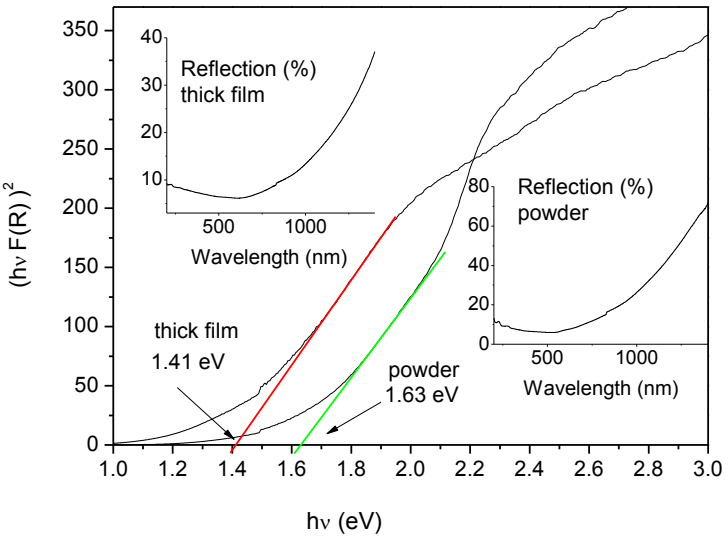

Fig. 4 Iron manganite powder and thick film Tauc plots and reflection spectra (insets)

3.2 Iron-manganite powder and thick film morphology and textural characteristics

SEM images of the synthesized $FeMnO_3$ powder show that it has a structure consisting of different sized particles, as shown on the inset in Fig. 5. This structure is typical for mechanochemical synthesis where the grain size distribution is often quite wide [33]. Polycrystalline aggregates can be noted and also very small nanosized particles. The overall mean particle size was determined as 534 nm, taking into account over 140 particles and aggregates observed in SEM images. The adsorption/desorption branches of the nitrogen isotherm obtained for iron manganite powder are almost overlapped as shown in Fig. 5, indicating a nonporous or macroporous nature of the obtained material (Type II isotherm by IUPAC nomenclature [36]). The slight increase in the region of relative pressure from 0.2 -0.9 also indicates the presence of some mesopores in the material. Their content is small, as indicated by the value 0.011 cm^3/g obtained by the Barret, Joyner and Halenda (BJH) method from the desorption branch of the isotherm. The specific surface area was calculated to be 6.3 m^2/g, from the measured N_2 physisorption isotherm using the Brunauer-Emmett Teller (BET) equation.

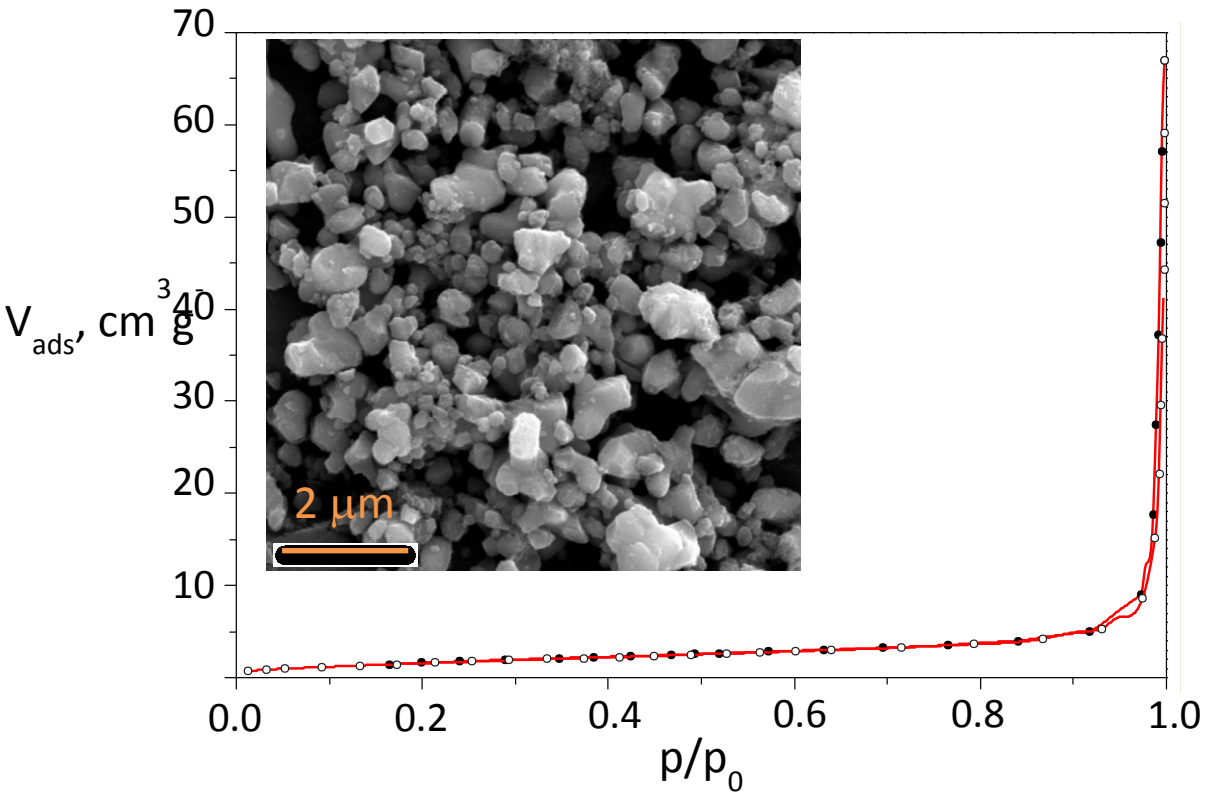

Fig. 5 SEM image and nitrogen adsorption/desorption isotherm obtained for $FeMnO_3$ powder

SEM images of the thick film sample surface are given in Fig. 6. The thick film surface consists of interconnected particles, relatively similar to the one obtained for freshly cleaved sintered bulk samples, as described in [21], reflecting the influence of the sintering process. Overall the particle size distribution is more homogenous.The small nanosized particles have sintered into larger particles and we can notice “necking” between individual particles characteristic for the intermediate stage of the sintering process. The average particle size (from over 300 particles) was determined to be 495 nm.

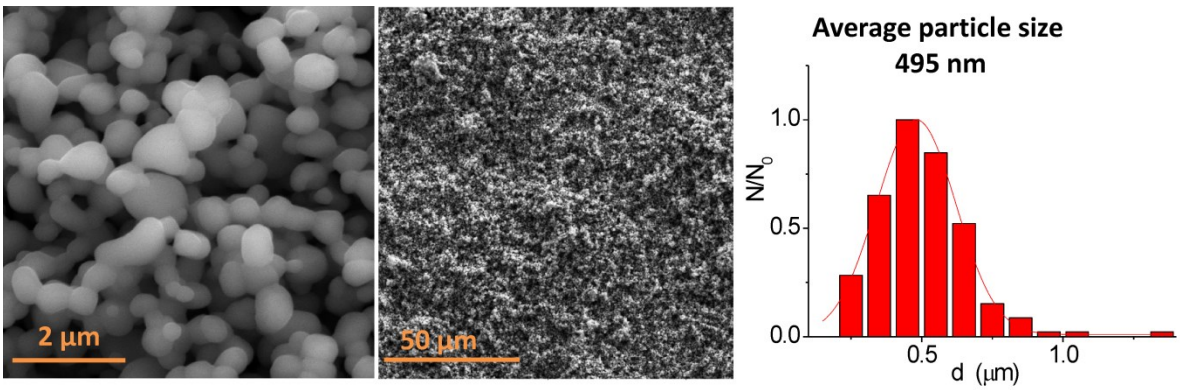

Fig. 6 SEM images of iron manganite thick film sample surface and particle size distribution (N/N_0 represents the number of particles of that size in relation to the total number of particles taken into account – over 300)

Integral and differential pore size distribution curves obtained from intrusion, as well as the textural parameters obtained from both Hg porosimetry measurements for iron manganite thick film samples, are given in Fig 7 and Table 1, respectively. Intrusion-extrusion curves of both runs (Run1 and Run2) are also presented as inserts in Fig. 7. Their shape similarity is obvious. In addition to similar values of the initial increase of the Hg intrusion volume, the most dominant characteristics of both curves are: a) sharp volume increase in the region of applied pressures greater than 2 MPa, b) almost no increase of the Hg imprinted volume in the region over 20 MPa, and c) branches of extrusion curves that are almost parallel by the corresponding intrusion curves.

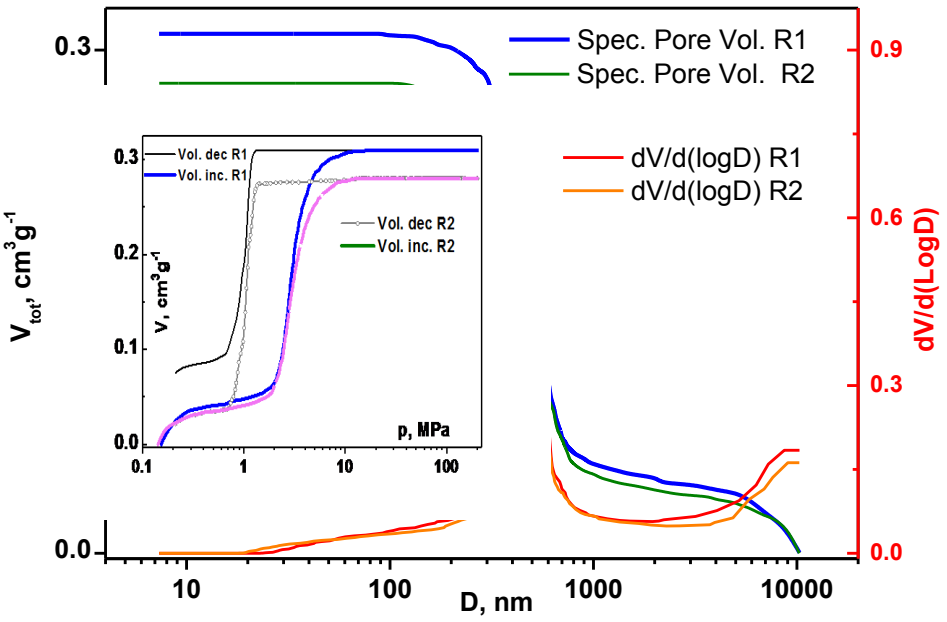

Fig. 7 Hg porosimetry measurements of thermally treated $FeMnO_3$ screen printed thick film samples on alumina substrate

Table 1 Parameters calculated from Hg porosimetry measurements for thermally treated $FeMnO_3$ thick film on alumina substrate and powder $FeMnO_3$.

	Thick film on alumina subs.		Powder calc.900 °C, 6h	
	Run1	Run2	Run1	Run2
[a] V_{tot}, (cm^3/g)	0.310	0.280	0.313	0.005
[b] SSA_{Hg}, (m^2/g)	2.5	2.3	4.4	0.3
[c] D_{ave}, (nm)	505	496	285.8	81.4
[d] D_{med}, (nm)	525	526	678	93
D_{max}, (nm) at dV/dlogD, (cm^3/g)	493 0.735	490 0.617	579 0.618	47 0.005

[e] ρ_{bulk}, (g/cm^3)	1.95	2.07	1.89	4.59
[f] ρ_{App}, (g/cm^3)	4.93	4.93	4.66	4.66
Porosity, (%)	60.6	58.0	61.7	2.4

[a]Total intruded Hg volume, [b]Specific surface area calculated for cylindric pore volume, [c]Average pore diameter 4V/S, [d]Mediana pore diameter at 50% of V_{tot}, [e]Bulk density obtained from Hg pycnometry at atmospheric pressure, [c]Apparent density obtained from intruded Hg volume at pressure of 200 MPa.

The parallelism observed for the intrusion-extrusion curves (also parallel to the y-axis) indicates a cylindrical pore system. This is not always the case as a similar curve shape can be found in non-porous systems of spherical particles [37]. The microstructure of the iron manganite thick film surface shown in Fig. 6 where particles and macropores are noticeable indicates that this is also not the case here.

The pore distribution curves shape for the initial pressure values of both runs indicates the possible presence of a macropore of diameter greater than 13 μm, which is the upper limit of pore diameter detection for the measurement procedure applied. On the other hand, the existence of a pore system in the region up to 800 nm is obvious, due to the upward trend of the integral pore distribution in both measurement cycles. The slightly lower values for Run 2 measurement in this region are probably due to the influence of increasing pressure on the rearrangement of the packing of sample components that entered into the dilatometer in the form of irregular plates. The sharp increase in volume corresponds to the most abundant pores, as evidenced by the distribution curve with a maximum at about 490 nm. The almost unchanged position of the maximum on the distribution curve of Run 2 *vs.* Run 1 indicates that this pore system is real, as it successfully resists possible compactification despite the applied pressure of 200 MPa during

Run1. Preservation of the pore system is documented by the closeness of the values of average pore diameter (D_{ave}) and median pore diameter (D_{med}) for both measurement cycles (Table 1). The total intruded volume of mercury for Run1 and Run2 also differ very little (0.31 vs 0.28 cm^3/g), significantly only in the region between 3-8 MPa while the shape of the curve is fully preserved. The difference in total porosity (60.6% vs 58.0%) and bulk density for both measurements originate dominantly from the difference in available pore volume in this region.

A particularly significant feature of the second run curve is that it shows that all mercury entering the material during the intrusion process exits it during the extrusion process. That would not be possible if the space into which mercury enters during intrusion, at least partly, originates from the voids between the particles. The equality of the total mercury volume in intrusion and extrusion branches of the curve of Run 2 is crucial evidence of the existence of a rigid system of pores in prepared iron manganite thick films. Finally, based on the differential distribution curve, it can be said that the pore system exists in the region from the largest diameters down to almost 20 nm. Pores with these diameters will not be involved in the capillary condensation process, but they ensure the effective transfer of water into the ceramic bulk [38].

In order to emphasize why it is significant to evaluate the porosity of actual thick film samples compared to powder, we performed Hg porosimetry measurements of two types of iron manganite powder (the synthesized powder used for making thick film paste, and also additionally calcined powder at 900 ^oC for 6h used to emulate the same conditions as thick film thermal treatment). Comparison of the results of Hg porosimetry measurements of synthesized powder, additionally calcined powder, and thick film samples enables an insight into the effect of the thick paste preparation method, screen printing and thermal treatment on the textural

characteristics of the sensor material. It also proves that application of Hg porosimetry on the powder for estimation of true textural parameters of the thick film material is not always valid.

Similar results were obtained for both analyzed powder samples, so we used the ones obtained for the additionally calcined powder. The SEM image (Fig. 8) of the additionally calcined $FeMnO_3$ powder shows that it has slightly more rounded particles compared to the synthesized powder, some "necking" between grains, but still slightly different from the thick film sample surface (Fig. 6). Integral and differential pore size distribution curves of the additionally calcined iron manganite powder for Run 1, as well as two inserts: intrusion-extrusion curve of both runs as a function of applied pressure (the left insert) and integral and differential pore size distribution curves of Run 2 (the right insert) are shown in Fig. 9. Comparing these results to the results obtained for thick film samples (Fig. 7) an obvious difference can be noticed, especially for Run 2 measurements.

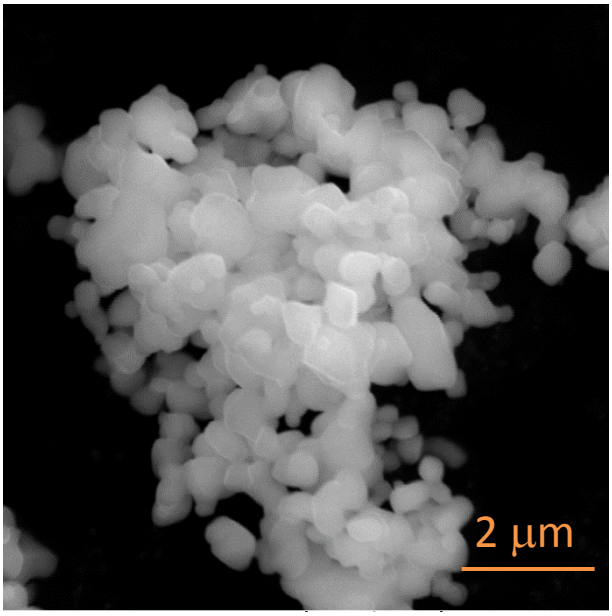

Fig. 8 SEM image of iron manganite powder additionally calcined at 900^{o}C for 6 h

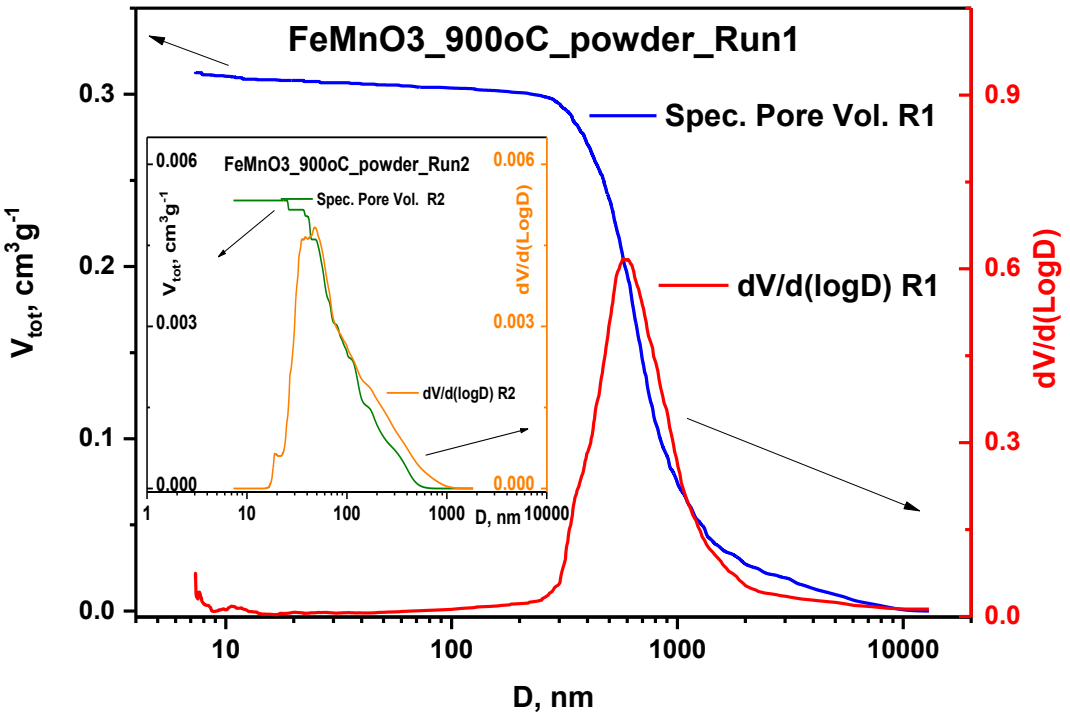

Fig. 9 Hg porosimetry measurements of additionally calcined $FeMnO_3$ powder

While the porous structure of the iron manganite screen-printed thick film samples is preserved, as can be seen through the significantly preserved reversibility of the extrusion branch of Run 1 and preserved values of all textural parameters obtained from Run 2 (Table 1), almost all texture diminishes after Run 1 for powder $FeMnO_3$. Indeed, the intrusion-extrusion curve of Run 2 of the powder material is hardly recognizable in the left insert on Fig 8, and the total intruded volume decreased over 60 times (from 0.313 to 0.005 cm^3/g). Additionally, integral and differential pore size distribution curves from Run 2, must be taken with great caution due to fact that the obtained signal is only 15% bigger than the signal obtained for the Hg compressibility measurement (blank measurement without sample). Some analytical improvement can be done by taking an around 20 times higher starting mass of powder for measurement to obtain the

signal to blank ratio ≥ 3:1. However, such a huge mass of the starting material will prevent achievable measurement of Run 1 due to the upper limit of the possible Hg intrusion volume during Run 1 (≈450 mm^3 for commercially dilatometers).

The huge reduction of V_{tot} value obtained for Run 2 of powder material clearly shows that compacting of the powder occurred during Hg intrusion process of Run 1. In other words, the measured V_{tot} from the Run 1 intrusion curve does not show the true pore structure but is a consequence of the existing interparticle space in the powder material. Particle space is also the reason for the SSA value calculated from Run 1 measurements for the powder sample (8.4 m^2/g for the synthesized powder and 4.4 m^2/g for the additionally calcined powder), which disappears during compacting process of Run 1 intrusion measurement causing the SSA value to drop (0.17 m^2/g for the synthesized powder and 0.3 m^2/g for the additionally calcined powder). Therefore, for each measurement of the powder material, which is later used to prepare the sensor by making a thick film paste, it is necessary to carry out successive second cycle measurements in order to evaluate the actual textural properties of that material. This is true also if the powder is treated in the same way as the thick film sample. This approach is extremely rarely applied in the results presented in the available literature. Of course, an even better approach is to measure two consecutive runs of prepared thick film paste film on the substrate, if possible, as obtained measurements will give information on the influence of the thick film preparation procedure on textural parameters of the final material.

In the case of our material the preparation procedure of thick film paste in combination with thermal treatment leads to obtaining a material with superior textural characteristics compared to the synthesized powder and also additionally calcined powder under the same thermal treatment conditions as thick film samples.

3.3 Influence of relative humidity on complex impedance

The dependence of complex impedance of iron manganite thick film samples on frequency in the analyzed relative humidity range 30-90% is shown in Fig. 10. The measured impedance (|Z|) decreased with increase in applied frequency and also decreased with increase in RH, where this difference is most expressed at lower measured frequencies (Fig. 10a). A similar change was noted for the real part of the complex impedance (Fig. 10b), while the change of the imaginary part of complex impedance (Fig. 10c) shows a peak shift towards higher frequencies both with working temperature increase, in accordance with the temperature-dependent relaxation process [25] and also as the relative humidity increases.

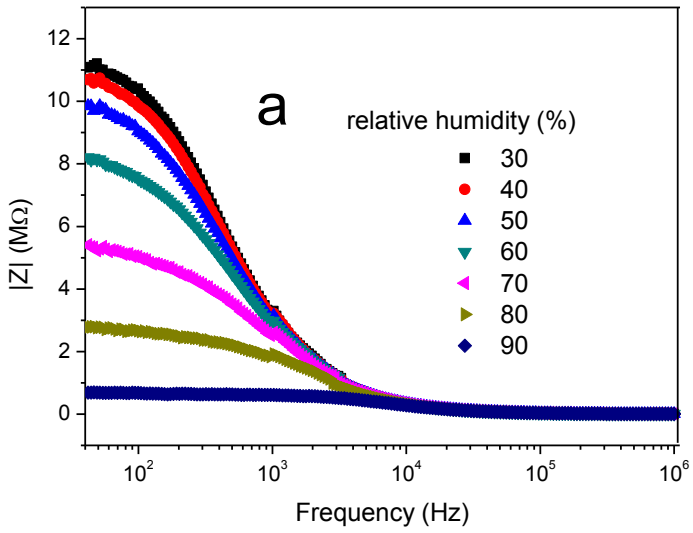

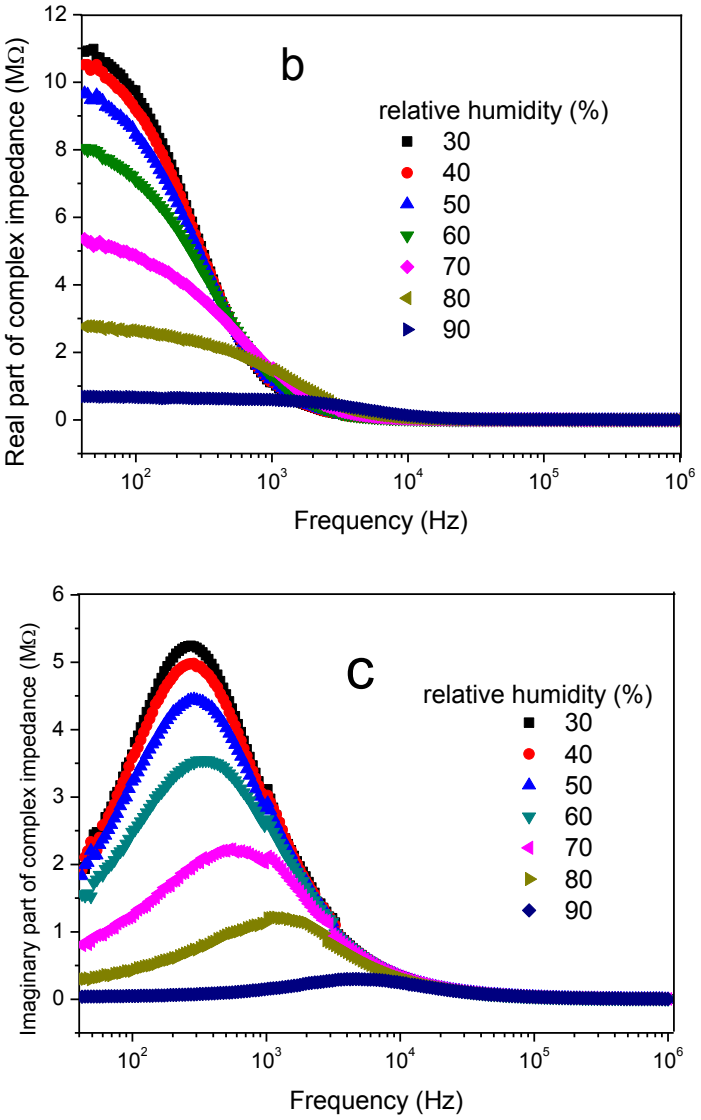

Fig. 10 Change of impedance (a), real (b) and imaginary (c) part of impedance with frequency in the RH range 30-90%

The change of impedance at several lower measured frequencies (50 Hz to 1 kHz) is shown in Fig. 11. Thus, at the frequency of 100 Hz the impedance |Z| reduced from 10.47 MΩ for RH of 30% to 0.68 MΩ for RH of 90%. At lower frequencies (50 and 100 Hz) it is noticeable that the slope of the decrease in impedance was gentler for lower relative humidity values (30-60%), and increased as the relative humidity increased.

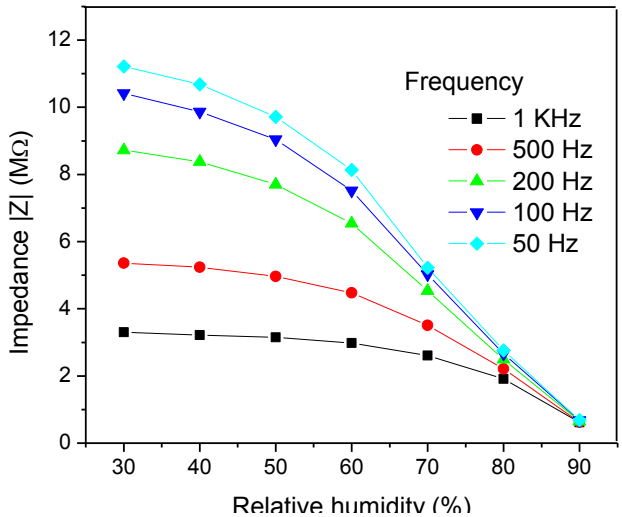

Fig. 11 Change of impedance of iron manganite thick film sample with relative humidity at different frequencies

The humidity sensitivity (S) for a given humidity range and at a set working frequency is determined as: $S = (|Z|_{LH} - |Z|_H) / |Z|_{LH} \times 100$, where $|Z|_{LH}$ is the value of impedance measured at the starting (lowest measured relative humidity - 30% in our case) and $|Z|_H$ is the impedance measured for different relative humidity values in the chamber. The calculated sensitivity for several frequencies is shown in Fig. 12.

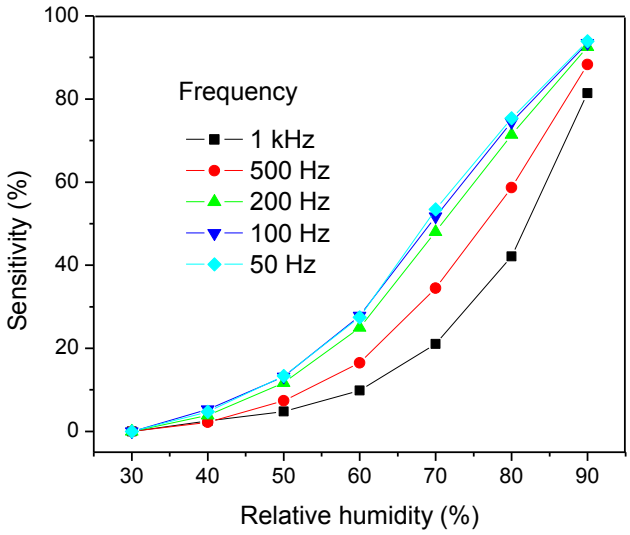

Fig. 12 Sensitivity curves of iron manganite thick film sample measured at different frequencies

As with impedance, we can note two sensitivity curves (more noticeable at 50 and 100 Hz) a gentler on for lower relative humidity (30-60%) and a more rapid one for higher relative humidity values between 60 and 90%. This is due to differences in the humidity sensing mechanism for lower and higher relative humidity levels, as explained in detail in [24]. At low relative humidity levels chemisorption of water molecules takes place on the surface of the sensor [10, 20]. A chemically adsorbed layer of OH^- ions forms bonded to metal (Fe, Mn) ions on the thick film sample surface [14]. As the relative humidity increases physisorption of water molecules takes place resulting in the formation of several absorbed layers of water (H_2O) molecules. Finally, for high relative humidity levels, water molecules are completely mobile, they move freely and occupy all pores with a mesopore radius above a certain value [20]. Both proton (H^+) hopping between adjacent adsorbed water molecules, better known as the Grotthus chain reaction and electrolysis of the condensed liquid take place [14]. This is why a good humidity sensing material needs to have a porous structure, such as the one obtained in this case iron manganite thick film samples which consisted of a network of particles and macropores. As described in detail above a detailed Hg porosimetry analysis of iron manganite thick film samples showed that they were highly porous (≈ 60%) with macropores with an average size of 500 nm and average particle size of 495 nm. Similar particle and pore sizes were obtained when we analyzed sintered bulk samples of iron manganite [21].

Measured complex impedance data (Fig. 13) was analyzed using an equivalent circuit consisting of a parallel resistance and constant phase element (CPE). The CPE was used to replace capacitance in order to take into account non-ideal Debye behavior [24, 31].

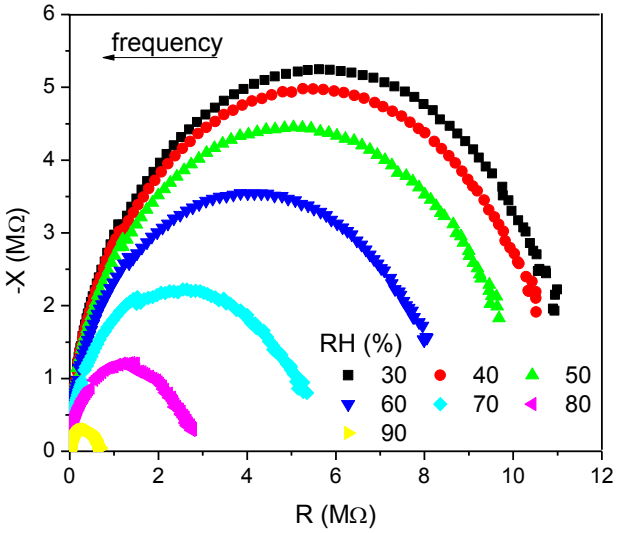

Fig. 13 Complex impedance diagrams measured at 25°C in the RH range 30-90%

An example of a fitted complex impedance curve for RH 40% is shown as an inset in Fig. 14. The values obtained for grain boundary resistance and relaxation frequency are shown in Fig. 14. Increase in RH led to a decrease in grain boundary resistance from 11.47 MΩ for RH 30% gradually to 8.42 MΩ for RH 60% and more rapidly as RH increased to 0.64 MΩ for RH 90%, while the relaxation frequency gradually moved from 1.7 kHz for RH 30% to 2.05 kHz for RH 60% and then to 29.4 kHz for RH 90%. This is in accordance with the change in impedance (Fig. 11) and sensitivity (Fig.12) and follows the mechanism of water interaction with the iron manganite thick film surface described above. The determined grain boundary capacitance was in the range 51.8 to 58.4 pF for RH 30-90%.

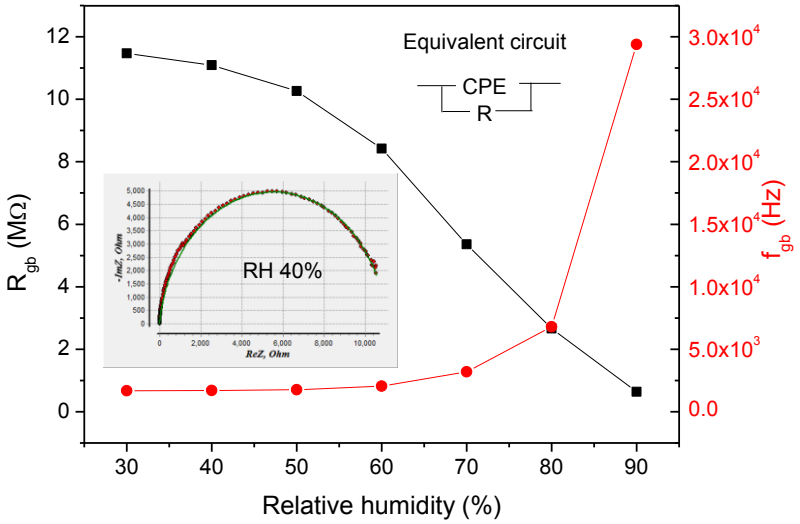

Fig. 14 Dependence of grain boundary resistance (a) and relaxation frequency (b) on RH; insets: example of fitted complex impedance curve for RH40% and equivalent circuit

3.4 Absorption/desorption -hysteresis

The time delay between absorption and desorption processes is defined as the hysteresis. If the hysteresis value is low then the sensor has good reversibility within the investigated humidity range. The determined hysteresis curve for iron manganite thick film sensor samples at the working frequency of 100 Hz is shown in Fig. 15. The calculated value was 2.8% over the whole analyzed relative humidity range confirming that iron manganite thick films can be applied for humidity sensing.

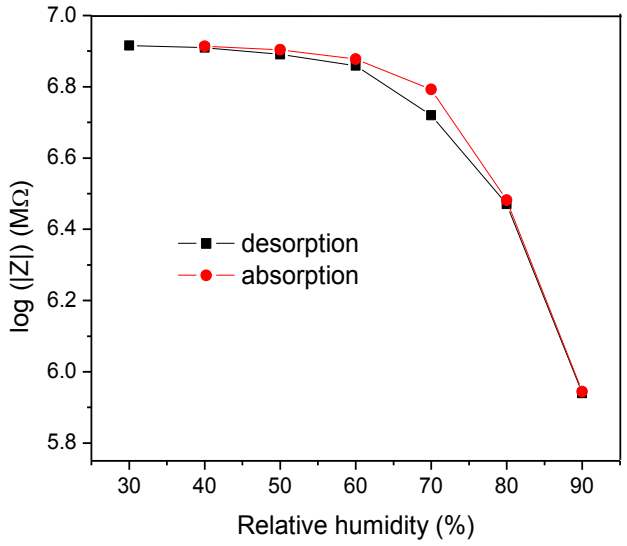

Fig. 15 Hysteresis curve for iron manganite thick film sample measured at 100 Hz

3.5 Response and recovery

Another important parameter for a good humidity sensor is the response and recovery time. The response time is the time the sensor needs to reach 90% of the total response when exposed to a certain relative humidity value, while the recovery time is the time the sensor needs to return to 90% of the starting baseline signal. The measured response and recovery times at 100 Hz for the relative humidity range 30-80% and 30-90% is shown in Fig. 16, where we can see that both response and recovery of iron manganite thick films is very short – several seconds, again confirming the potential of iron manganite thick films as a sensing material.

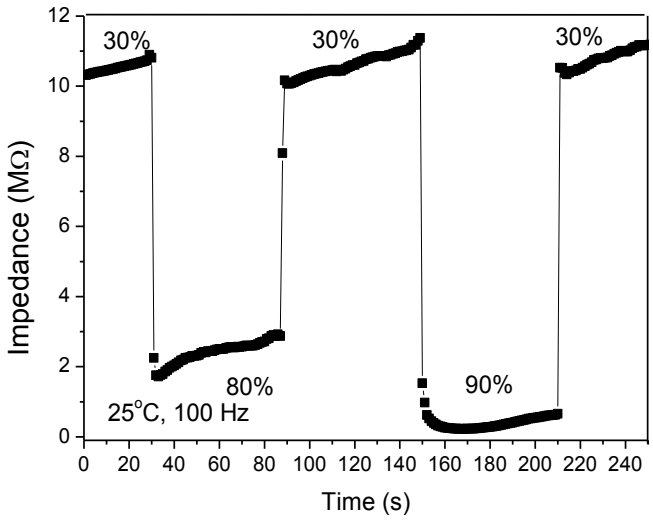

Fig. 16 Response and recovery times of iron manganite thick film sensor sample at 100 Hz from RH 30 to RH 80 and 90%

4. Conclusion

Iron manganite thick film samples were investigated in view of potential application as humidity sensors. They were obtained by screen printing four layers of iron manganite paste on alumina substrate with test interdigitated PdAg electrodes, heat-treated at 900^{o}C for 6h. Structural, morphological and textural analysis of thick films using XRD, SEM and Hg porosimetry showed that pure iron manganite thick films were obtained with an average particle size of 495 nm, with high porosity (60.6%) with a similar average pore size (500 nm) and high carrier mobility of 55.18 cm^2/V·s. Hg porosimetry was measured on starting powder, additionally calcined powder and thick film samples showing that true textural parameters of the thick film can be obtained for measurements of actual thick film samples. The measured impedance decreased noticeably with increase in relative humidity, hysteresis values were low (2.8%). The response and recovery times were also relatively short showing that this mixed metal oxide with a cubic bixbyite

structure has potential for application in humidity sensing. Further work will focus on testing this promising multi metal oxide material to other gases and its selectivity towards gas mixtures.

Acknowledgements

The authors would like to express their gratitude to Dr. M. Mitric for XRD measurements of iron manganite powder samples. This work was performed as part of projects III45007, III45014 and III45001 financed by the Ministry for Education, Science and Technological Development of the Republic of Serbia.

Data availability statement

Some of the raw/processed data required to reproduce these findings cannot be shared at this time due to technical or time limitations, while some of it is part of an ongoing study

References

1. S. Hanif, A. M. Khedr, Z. Al Aghbari, D. P. Agrawal, Opportunistically exploiting Internet of Things for wireless sensor network routing in Smart Cities, J. Sens. Actuator Netw. 7 (2018) 461.
2. N. Khalil, M. R. Abid, D. Benhaddou, Wireless sensor network for Internet of Things, Proceedings of the IEEE Ninth International Conference on Intelligent Sensors, Sensor Networks and Information Processing (ISSNI), (2014) 1-4.
3. M. S. Khan, M. S. Islam, Design of a reconfigurable RFID sensing tag as a generic sensing platform toward the future Internet of Things, IEEE Internet of Things Journal, 1 (2014) 300-310.

4. G. F. Fine, L. M. Cavanagh, A. Afonja, R. Binions, Metal oxide semi-conductor gas sensors in environmental monitoring, Sensors, 10 (2010) 5469-5502.
5. A. Dey, Semiconductor metal oxide gas sensors: A review, Mat. Sci. Eng. B 229 (2019) 206-217
6. H. Nazemi, A. Joseph, J. Park, A. Emadi, Advanced micro- and nano-gas sensor technology: A review, Sensors, 19 (2019) 1285
7. D. Zappa, V. Galstyan, N. Kaur, H. M. M. M. Arachchige, O. Sisman, E. Comini, Metal-oxide – based heterostructures for gas sensors – A review, Analytica Chimica Acta 1039 (2018) 1-23
8. H. Faharani, R. Wagiran, M. N. Hamidon, Humidity sensors principle, mechanism and fabrication technologies: A comprehensive review, Sensors, 14 (2014) 7881-7939, 2014
9. J.-M. Tulliani, C. Baroni, L. Zavattaro, C. Grignani, Strontium-doped hematite as a possible humidity sensing material for soil water content determination, Sensors, 13 (2013) 12070-12092
10. T. Scherban, A. S. Nowick, Bulk protonic conduction in Yb-doped $SrCeO_3$, Solid State Ion. 35 (1989) 189-194
11. C. Moure, O. Pena, Recent advances in perovskites: Processing and properties, Prog. Solid State Ch. 43 (2015) 123-148
12. A. Tripathy, S. Pramqanik, A. Manna, S. Bhuyan, N. F. A. Shah, Z. Radzi, N. A. A. Osman, Design and development of capacitive humidity sensor applications of lead-free Ca, Mg, Fe, Ti-oxides based electro-ceramics with improved sensing properties via physisorption, Sensors 16 (2016) 1135

13. L. M. Feng, L. Q. Jiang, M. Zhu, H. B. Liu, X. Zhou, C. H. Li, Formability of ABO_3 cubic perovskites, J. Phys. Chem. Solids 69 (2008) 967-974
14. M. Viviani, M. T. Buscaglia, V. Buscaglia, M. Leoni, P. Nanni, Barium perovskites as humidity sensing materials, J. Eur. Ceram. Soc, 21 (2001) 1981-1984
15. C. Doroftei, P. D. Popa, F. Iacomi, Study of the influence of nickel ions substitutes in barium stannates used as humidity resistive sensors, Sens. Actuators A:Phys. 173 (2012) 24-29
16. A. J. Reynolds, J. C. Conboy, Barium titanate nanoparticle based nonlinear optical humidity sensor, Sens. Actuators B:Chem, 273 (2018) 921-926
17. S. Rayaprol, S. D. Kaushik, Magnetic and magnetocaloric properties of $FeMnO_3$, Ceram. Int. 41 (2015) 9567-9571
18. D. Gosh, U. Dutta, A. Haque, N. E. Morvidonova, O. I. Lebedev, K. Pal, A. Gayen, P. Mahata, A. K. Kundu, Nd. M. Seikh, Evidence of low temperature spin glass transition in bixbyite type $FeMnO_3$, Mater. Sci. Eng. B 226 (2017) 206-210
19. B. Kolk, A. Albers, I. R. Leith, M. G. Howden, Mössbauer and X-ray studies of the structure of iron-manganese oxide catalyst precursors, Applied Catal. 37 (1988) 57-74
20. L. Leontie, C. Doroftei, A. Carlescu, Nanocrystalline iron manganite prepared by sol-gel self-combustion method for sensor application, Appl. Phys. A, 124 (2018) 750
21. M. V. Nikolic, M. D. Lukovic, N. J. Labus, Influence of humidity on complex impedance and dielectric properties of iron manganite ($FeMnO_3$), J. Mater. Sci.: Mater. Electron. 30 (2019) 12399-12405

22. M. V. Nikolic, M. D. Lukovic, M. Dojcinovic, Z. Z. Vasiljevic, N. J. Labus, Application or iron manganite thick films for humidity sensing, Proceedings of the International Spring Seminar on Electronics Technology, Volume 2019, May 2019, 8810291
23. S. Ito, P. Chen, P. Comte, M. K. Nazeruddin, P. Liska, P. Pechy, M. Graetzel, Fabrication of screen-printing pastes from TiO_2 powders for dye-sensitized solar cells, Prog. Photovolt. Res. Appl. 15 (2007) 603-612
24. M. V. Nikolic, Z. Z. Vasiljevic, M. D. Lukovic, V. P. Pavlovic, J. Vujancevic, M. Radovanovic, J. B. Krstic, B. Vlahovic, V. B. Pavlovic, Humidity sensing properties of nanocrystalline pseudobrookite (Fe_2TiO_5) based thick films, Sens. Actuators B. Chem. 277 (2018) 654-664
25. S. Gowreesan, A. Ruban Kumar, Structural, magnetic and electrical property of nanocrystalline perovskite structure of iron manganite ($FeMnO_3$), Appl. Phys. A, 123 (2017) 689
26. B. H. Toby, R. B. Von Dreele, GSAS II the genesis of a modern open-source all purpose crystallography software package, J. Appl. Crystallogr. 46 (2) (2013) 544-549
27. I. C. Cosentino, E. N. S. Muccillo, R. Muccillo, Development of zirconia-titania porous ceramics for humidity sensors, Sens. Actuators B:Chem., 96 (2003) 677-683
28. G. B. Crochemore, A. R. P. Ito, C. A. Goulart, D. P. F. D. Souza, Identification of humidity sensing mechanism in $MgAl_2O_4$ by impedance spectroscopy as a function of relative humidity, Mater. Res. 21 (2018), 1-9
29. I. Cosentino, E. N. S. Muccillo, R. Muccillo, The influence of Fe_2O_3 in the humidity sensor performance of ZrO_2:TiO_2-based porous ceramics, Mater. Chem. Phys. 103 (2007) 407-414

30. I. Hadzaman, O. Shpotyuk, M. Brunner, Integrated thick-film nanostructures based on spinel ceramics, Nanoscale Res. Lett. 9 (2014) 149
31. M. V. Nikolic, Z. Z. Vasiljevic, M. D. Lukovic, V. P. Pavlovic, J. B. Krstic, J. Vujancevic, N. Tadic, B. Vlahovic, V. B. Pavlovic, Investigation of $Zn_2Fe_2O_4$ spinel ferrite nanocrystalline screen-printed thick films for application in humidity sensing, Int. J. Appl. Ceram. Technol. 16 (2019) 981-993
32. D. Seifu, A. Kebede, F. W. Oliver, E. Hoffman, E. Hammond, C. Wynter, A. Aning, L. Takacs, I. –L. Siu, J. C. Walker, G. Tessema, M. S. Seehra, Evidence of ferrimagnetic ordering in $FeMnO_3$ produced by mechanical alloying, J. Magn. Magn. Mater. 212 (2000) 178-182
33. I. Malaescu, A. Lungu, C. N. Marin, P. Vlazan, P. Sfirloaga, G. M. Turi, Experimental investigations of the structural transformations induced by the heat treatment in manganese ferrite synthesized by ultrasonic assisted co-precipitation method, Ceram. Int. 42 (2016) 16744-16748
34. S. N. de Medeiros, A. Luciano, L. F. Cotica, I. A. Santos, A. Paesano Jr, J. B. M. da Cunha, Structural and magnetic characterization of the ball-milled α-Fe_2O_3-Mn_2O_3 and α-Fe-MnO_3 systems, J. Magn. Magn. Mater. 281 (2004) 227-233
35. M. H. Habibi, V. Mosavi, Wet coprecipitation preparation of perovskite-type iron manganite nano powder pure phase using nitrate precursors: structural, opto-electronic, morphological and photocatalytic activity for degradation of Nile blue dye, J. Mater. Sci.:Mater. Electron. 28 (2017) 10270-10276
36. M. Thommes, K. Kaneko, A. V. Neimark, J. P. Olivier, F. Rodriguez-Reinoso, J. Ronquerol, K. S. W. Sing, Physisorption of gases, with special reference to the evaluation

of surface area and pore size distribution (IUPAC Technical Report), Pure Appl. Chem. 87 (2015) 1051-1069

37. W. K. Bell, J. Van Brakel, P. M. Heertjes, Mercury penetraton and retraction hysteresis in closely packed spheres, Powder Technology, 29 (1981), 75-88
38. H. Klym, I. Hadzaman, O. Shpotyuk, M. Brunner, Integrated thick-film nanostructures based on spinel ceramics, Nanoscale Research Letters, 9 (2014) 149